

Deposition of Nanostructured Fluoropolymer Films on Silicon Substrates via Plasma Polymerization of Allylpentafluorobenzene

G. D. Fu, E. T. Kang,* and K. G. Neoh

Department of Chemical Engineering, National University of Singapore, Kent Ridge, Singapore 119260

Received: August 25, 2003; In Final Form: October 22, 2003

Nanostructured fluoropolymer films were deposited via plasma polymerization of allylpentafluorobenzene (APFB) on pristine (native oxide-covered) Si(100) and hydrogen-terminated Si(100) (H-Si) surface. By changing the substrate temperature, radio frequency (RF) power, and system pressure, fluoropolymer films composed of fairly well-defined and uniform nanospheres were deposited. The size and size distribution of the nanospheres in the deposited films was studied by atomic force microscopy (AFM) and scanning electron microscopy (SEM). Under the high RF power (400 W) and high system pressure (800 mTorr), nanoporous fluoropolymer films composed of spheres with mean diameter (D_m) on the order of 120 nm and narrow size distribution (standard deviation in diameter, $SD \sim 9$ nm) were obtained. The chemical composition and structure of the nanostructured films were studied by X-ray photoelectron spectroscopy (XPS), time-of-flight secondary ion mass spectrometry (ToF-SIMS), and Fourier transform infrared (FTIR) spectroscopy. The fluoropolymer films were highly hydrophobic in nature and could give rise to surface water contact angles above 150° . Although the morphology of the fluoropolymer films deposited on both types of silicon substrates was similar, chemical interaction at the polymer/H-Si interface had resulted in stronger adhesion of the fluoropolymer film to the silicon substrate.

1. Introduction

Ultralow dielectric constant interlayers are required to reduce the RC time delay, cross talk, and power dissipation in the new generation of high density integrated circuits.^{1–4} Fluoropolymers are potential materials for interlayer dielectric applications because of their low dielectric constants and good chemical and thermal stability.⁵ However, their applications in the submicron and nano-level electronics are hindered by difficulties in processing.⁶ On the other hand, plasma polymerization has been shown to be a convenient way for depositing polymer and fluoropolymer films of controlled composition and properties on assorted substrates in the absence of a solvent.^{7–17} Hence, the processing problem of fluoropolymers can be partially overcome by plasma polymerization and deposition. A number of studies have been devoted to the plasma polymerization of fluorine-containing monomers to produce low dielectric constant materials.^{14,18–20}

In recent years, the introduction of air gaps into interconnect structures^{21,22} and nanopores into polymers^{23–25} has become an attractive approach to reducing their dielectric constants. The incorporating of air which has a dielectric constant of about 1 can substantially reduce the dielectric constant of the resulting porous structure. Fine works on the preparation of low dielectric constant poly(silsesquioxane)s,^{26,27} polyimides,^{23,28–31} and organosilicates^{24,32} have been reported. The generation of particles with size ranging from nanometers to submicrometers in the gas-phase plasma deposition process under high RF power and high pressure is a well-known phenomenon. A number of studies have been devoted to the elucidation of the mechanisms^{33–36}

and the use of glow discharge to produce nanoscale particles.^{37–39} When particles agglomerate to form a film, interstitial spaces are formed. Thus, films fabricated from nanospheres are in reality a nanoporous material. Accordingly, plasma polymerization and deposition of spherical nanoparticles offer an opportunity for preparing nanostructured and nanoporous fluoropolymer films.

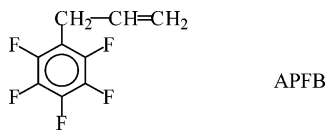
In this work, 1-allylpentafluorobenzene was used as the monomer for the plasma polymerization and deposition of nanostructured fluoropolymer films on pristine (native oxides-covered) and hydrogen-terminated Si(100) surfaces. By careful selection of the glow discharge parameters, nanostructured fluoropolymer films composed of spherical nanoparticles with mean diameters ranging from 120 to 700 nm were prepared. The morphology of the films was revealed by scanning electron microscopy (SEM) and atomic force microscopy (AFM). The chemical composition and structure of the fluoropolymer films were studied by X-ray photoelectron spectroscopy (XPS), Fourier transform infrared (FTIR) spectroscopy, and time-of-flight secondary ion mass spectrometry (ToF-SIMS).

2. Experimental Section

2.1. Materials. (100)-Oriented single-crystal silicon wafers, having a thickness of about 0.65 mm and a diameter of 150 mm, were obtained from Unisil Co. of Santa Clara, CA. The as-received wafers were polished on one side and doped as p-type. The Si wafers were sliced into square chips of about 5 mm \times 5 mm in dimension. To remove the organic residues on the surface, the silicon substrates were washed with the “piranha” solution, a mixture of 98 wt % concentrated sulfuric acid (70 vol %) and hydrogen peroxide (30 vol %). After rinsing with copious amounts of doubly distilled water, the Si substrates

* To whom correspondence should be addressed. Phone: +65-68742189. Fax: +65-67791936. E-mail: cheket@nus.edu.sg.

were dried in an argon stream. The monomer, 1-allylpentafluorobenzene (APFB) used for plasma polymerization was obtained from the Aldrich Chemical Co. of Milwaukee, WI. The chemical structure of APFB is shown below:



2.2. Preparation of the Hydrogen-Terminated Si(100) Surface: The H-Si Surface. A 10 vol % hydrofluoric acid solution was deoxygenated by sparging with argon for about 30 min through a Teflon tube inserted into the solution. The pristine (native oxide-covered) silicon chips were immersed in the hydrofluoric acid (HF) solution in individual Teflon vials. A 5 min immersion time was sufficient to remove the oxide film and to leave behind a uniform hydrogen-terminated Si(100) surface (H-Si surface).⁴⁰ The silicon chip was washed with copious amounts of argon-purged ethanol.

2.3. Plasma Polymerization and Deposition of APFB: The pp-APFB Films. Plasma polymerization and deposition on pristine Si and H-Si surfaces were carried out on the Plasma 80 Plus PECVD system, manufactured by Oxford Instruments Plasma Technology Inc. of Yatton, U.K. The radio frequency (RF) generator was operated at a frequency of 13.56 MHz. The plasma deposition process was performed between two parallel plate electrodes of 24 cm in diameter and 6 cm apart. The silicon chips were placed on the ground electrode. Prior to each experiment, the deposition chamber was purged with argon at a flow rate of 30 standard cubic centimeters per min (sccm) and under a system pressure of 600 mTorr. A cleaning/etching operation by argon plasma was subsequently performed under room temperature at the system pressure of 600 mTorr and RF power of 30 W for about 1 min. The APFB monomer was introduced into the deposition chamber by an argon carrier gas stream. The gas stream was allowed to flow through the system at 30 sccm for about 2 min, prior to ignition of the glow discharge at a predetermined RF power, substrate temperature, and system pressure. In all cases, the carrier gas stream was assumed to be saturated with the APFB monomer. After the deposition process, the system was purged with argon for 5 min.

2.4. Thickness Measurement and Deposition Rate of the pp-APFB Film. The thickness of the pp-APFB films was determined using an Alpha-STEP 500 surface profiler. For thinner films, the thickness was also checked on the Nanospec/AFM system, manufactured by Nanometrics Co. of Sunny Vale, CA. The deposition rate was determined by measuring the thickness of the pp-APFB film as a function of time. For the pp-APFB film deposited at the RF power of 400 W, a system pressure of 800 mTorr, and a substrate temperature of 25 °C, the thickness of the film increases linearly at a rate of about 0.7 $\mu\text{m}/\text{min}$ during the first min. The rate of deposition (the increase in film thickness) decreased to and remained at about 0.4 $\mu\text{m}/\text{min}$ subsequently, probably due to the onset of the etching effect of the plasma.

2.5. Adhesion Strength Measurements. The adhesion strength of the pp-APFB films with pristine Si and H-Si substrates was evaluated by the 180°-peel adhesion test. Scotch tape was applied to the pp-APFB film on the Si substrate and subsequently peeled off on an Instron 5544 tensile tester of the Instron Corporation of Caton, MA. All measurements were carried out at a cross-head speed of 10 mm/min. For each peel adhesion strength reported, at least three sample measurements with variation within ± 0.3 N/cm were averaged. The chemical

composition of the delaminated interfaces was analyzed by X-ray photoelectron spectroscopy.

2.6. Characterization of the Surface Morphology of the pp-APFB Films. The surface morphology of the pp-APFB films was studied by atomic force microscopy (AFM), using a Nanoscope IIIa AFM from the Digital Instruments Inc. In each case, an area of $5\ \mu\text{m} \times 5\ \mu\text{m}$ was scanned using the tapping mode. The drive frequency was 330 ± 50 kHz, and the voltage was between 3 and 4.0 V. A drive amplitude of 300 mV, a set point of 3.34 μV , and a scan rate of 1.0 Hz were used. The arithmetic mean of the surface roughness (R_a) was calculated from the roughness profile.

Scanning electron microscopy (SEM) measurements were carried out on a JEOL 6320 scanning electron microscope at an accelerating voltage of 15 kV. The particle size and size distribution were derived from the SEM images. The mean diameter (D_m) of the particles was calculated from the following relationship:

$$D_m = (\sum_{i=1}^n D_i)/n$$

in which D_i is the diameter of a particle and n is the total number of the particles. In this study, 100 particles were chosen arbitrarily for each pp-APFB film. The standard deviation in diameter (SD) was used as a measure of the size distribution of the particles. It was calculated from the following relationship:

$$\text{SD} = \sqrt{(\sum_{i=1}^n (D_i - D_m)^2)/n}$$

2.7. Characterization of the Chemical Composition and Structure of the pp-APFB Films. X-ray photoelectron spectroscopy (XPS) measurements were made on a Kratos AXIS HSi spectrometer (Kratos Analytical Inc., Manchester, England) with a monochromatized Al K α X-ray source (1456.6 eV photons), under conditions similar to those described earlier.^{41,42} Time-of-flight secondary ion mass spectrometry (ToF-SIMS) analysis was carried out on an ION-TOF SIMS IV instrument (ION-TOF, GmbH, Germany), using procedures similar to those described earlier.^{41,42} The primary ion beam (10 keV Ar⁺) with a spot size of $\sim 50\ \mu\text{m}$ was rastered over an area of $500 \times 500\ \mu\text{m}^2$ while keeping the total dose under 10^{13} ions/cm².

The pp-APFB samples for Fourier transform infrared (FTIR) spectroscopy measurements were obtained by direct plasma polymerization and deposition of APFB on the freshly pressed KBr pellets at the system pressure of 800 mTorr, Ar flow rate of 30 sccm, and substrate temperature of 25 °C for about 2 min. The RF power was varied from 100 to 400 W. The FTIR spectra were recorded in air on a Bio-Rad FT-IR, model 400, spectrophotometer. Each spectrum was collected by accumulating 30 scans at a resolution of 8 cm⁻¹.

2.8. Water Contact Angle Measurements. The advancing and receding water contact angles were measured at 25 °C and 50% relative humidity on a telescopic goniometer (Rame-Hart, model 100-00(230), Mountain Lake, NJ). The telescope with a magnification power of 23 \times was equipped with a protractor of 1° graduation. For each angle reported, at least five readings from different surface locations were averaged.

3. Results and Discussion

The morphology, particle size, particle size distribution, chemical composition, and chemical structure of the fluoropoly-

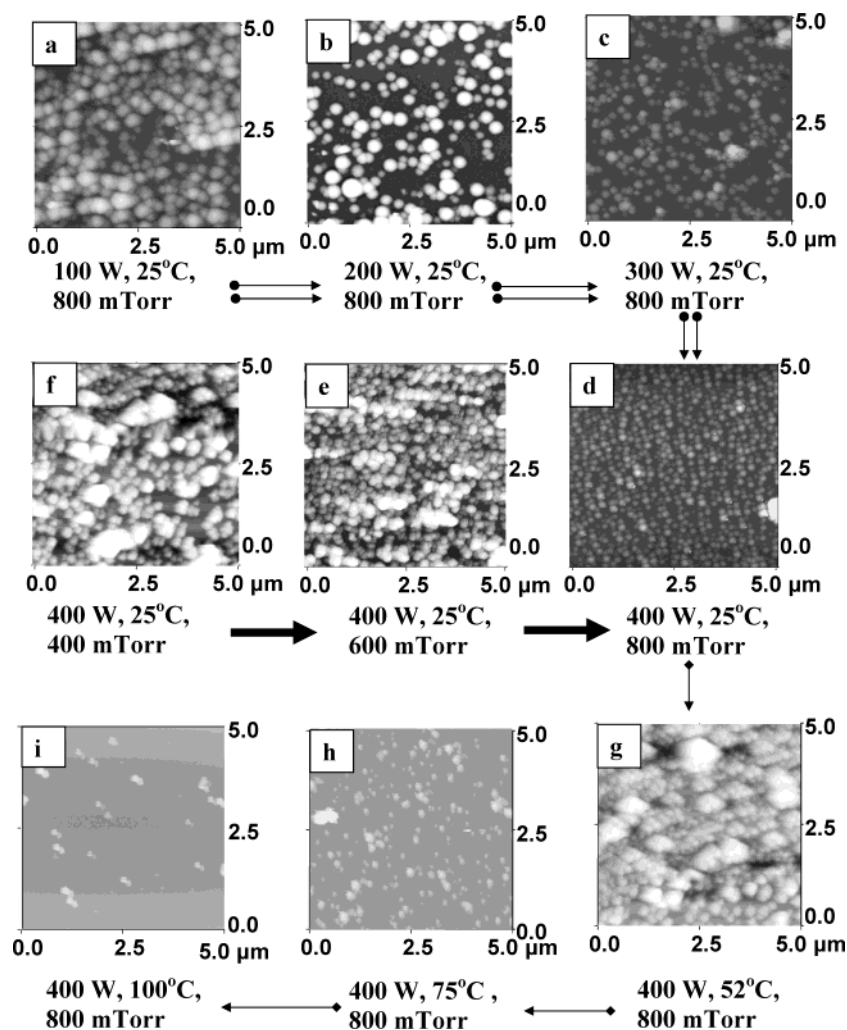


Figure 1. $5 \times 5 \mu\text{m}$ AFM images of the pp-APFB films deposited under various glow discharge conditions.

mer films obtained from the plasma polymerization process are dependent on the glow discharge parameters, such as the deposition time, RF power, system pressure, and substrate temperature.^{35,36} The size of the particle was found to be dependent on the deposition time. The longer the time duration, the larger the particles size.³⁵ Short and continuously pulsed plasma polymerization of the fluoromonomer on the minute time scale led to nanospheres deposition.³⁷ On the other hand, the size and surface distribution of occlusions from pulsed plasma were found to be monomer dependent. In the present work, the effect of plasma deposition time will not be studied further. The glow discharge time will be fixed at 1 min for depositions carried out on both types of the silicon substrates.

3.1. Morphology of the Nanostructured pp-APFB Films. For the plasma polymerization of 1-allylpentafluorobenzene (APFB), the system pressure, substrate temperature, and the RF power can be used to regulate the particle size and particle size distribution. The mean diameter (D_m) and the corresponding standard deviation in particle diameter (SD) of the plasma-polymerized APFB (pp-APFB) films deposited over a range of system pressure and RF power on the pristine (native oxide-covered) silicon substrates are summarized in Table 1. The temperature of the substrates was kept at 25 °C.

The data in Table 1 suggest that increasing the RF power used for deposition reduces the mean diameter of the deposited particles and their size distribution. At room temperature and under the high system pressure of 800 mTorr, the D_m of the particles in the pp-APFB film decreases from 534 to 120 nm,

TABLE 1: Mean Diameters and Size Distribution of the Particles in the pp-APFB Films Obtained at Different RF Power and System Pressure on Pristine Si(100) Substrates

RF power (W)	mean particles diameter, D_m (nm)				standard deviation, SD (nm)			
	200 mTorr	400 mTorr	600 mTorr	800 mTorr	200 mTorr	400 mTorr	600 mTorr	800 mTorr
100	714	736	700	534	128	146	80	60
200	500	383	373	342	100	74	65	50
300	334	303	251	165	80	79	68	24
400	264	272	166	119	72	79	16	9

when the RF power is increased from 100 to 400 W. At the same time, the SD of the particles in the corresponding films decreases from 60 to 9 nm. The size of the spherical particles deposited under the RF powers of 100, 200, 300, and 400 W are revealed by the AFM images of the respective pp-APFB films in Figure 1a–d. The decrease in size and size distribution of the nanoparticles with the increase in RF power can be explained by the “killer particulates” theory.⁴⁰ Particles from plasma processing originate either from gas phase nucleation (homogeneous growth) or from fractured films deposited on the substrate surface (heterogeneous growth). At the high RF power, such as 400 W, a high concentration of radicals and ions are created in the gas phase. Under this condition, the gas phase reaction among the radicals and other active species are favored. As a result, most of the particles are formed by homogeneous nucleation. At the low RF power, for example at 100 W, the particles are generated not only in the gas-phase reactions but

also on the surface. Thus, the particles obtained at the low RF power are not as uniform in size as those obtained at the high RF power. Furthermore, at the high RF power, the system will have more reactive species which can lead to more nucleation sites. Because the total amount of monomer remains constant under a given gas flow rate and system pressure, more nucleation sites will lead to smaller particles.

The data in Table 1 also indicate that not only does the system pressure have an effect on the size of the particles but it also controls the particle size distribution. At the low RF power (100 W), the effect of system pressure on the particle size and particle size distribution is less obvious than that at the high RF power (400 W). At the RF power of 400 W, and with the system pressure increasing from 200 mTorr to 800 mTorr, the D_m of the particles decreases from 264 to 120 nm, whereas the SD decreases from 72 to 9 nm. At the RF power of 100 W, the D_m decreases from 714 to 514 nm and the corresponding SD decreases from 128 to 60 nm. The smaller size and narrower size distribution of the spherical nanoparticles obtained at the high pressure and high RF power can be accounted for as follows. First of all, the APFB monomer is a high boiling point liquid (bp 148–149 °C under atmosphere conditions). Because the liquid monomer reservoir and the plasma chamber were connected and maintained at the same pressure, decreasing the system pressure will result in an increase in the volumetric flow rate of the APFB-carrier gas stream and vice versa. Thus, an increase in system pressure will lower the effective concentration of APFB within the glow discharge chamber. This effect will give rise to a reduction in particle size and size distribution at a fixed RF power. Variation in monomer concentration at a fixed pressure has been shown to have the similar effect on particle size and size distribution. Figure 1 also shows the AFM images of the plasma polymerized and deposited films obtained under the constant temperature of 25 °C and constant RF power of 400 W, but at the system pressure of 400 mTorr (part d), 600 mTorr (part e), and 800 mTorr (part f). Thus, increasing the system pressure is advantageous to the formation of well-defined nanospheres. The large particles of irregular size and shape, obtained at the low system pressure, were formed by the increased collision and aggregation of nucleation sites.

The particle size and size distribution, and thus the topography of the pp-APFB film, are also affected by the substrate temperature. The AFM images of the pp-APFB film obtained at the system pressure of 800 mTorr and constant RF power of 400 W, but at substrate temperatures of 52, 75, and 100 °C, are shown in Figure 1g–i, respectively. A high substrate temperature is disadvantageous to the generation of the spherical nanoparticles. A high substrate temperature will increase the surface mobility and the diffusion length of the deposited species. These effects, which favor surface rearrangements, will lead to a denser film with less well-defined surface features. Furthermore, an increase in substrate temperature reduces the probability for nucleation, causing delays in the appearance of the particles.²⁰

Fluoropolymer films composed of uniform and well-defined nanospheres are deposited under the conditions of high RF power, high system pressure and low substrate temperature. Figure 2a shows the AFM topographical image of the pp-APFB film deposited on the pristine (oxide-covered) Si surface at the substrate temperature of 25 °C, system pressure of 800 mTorr and RF power of 400 W. This pp-APFB film is composed of nanospheres of about 120 nm in mean diameter. The two-dimensional image of the corresponding film surface is shown in Figure 1d. Because of the high surface roughness value and

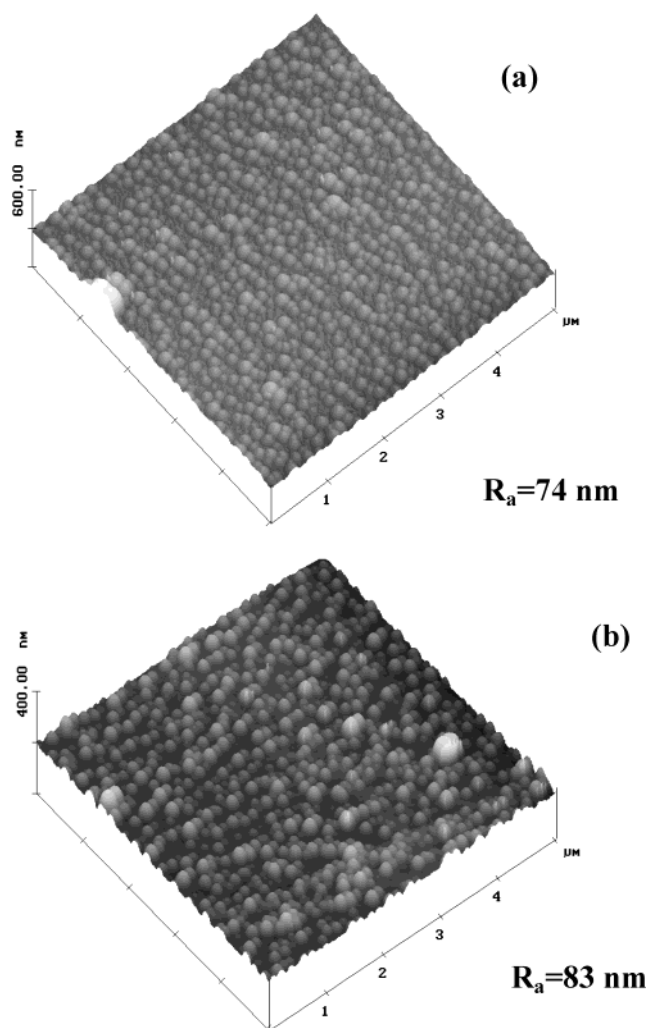


Figure 2. AFM topographical image of the pp-APFB films deposited at 400 W, 800 mTorr, and 25 °C on the (a) pristine silicon (native oxide-covered) surface and (b) hydrogen-terminated silicon surface.

the limited contrast in the two-dimensional AFM image, the presence of full surface coverage by the nanospheres is revealed unambiguously only in the topographical image of Figure 2a. Although the chemical states of the silicon surface have a profound effect on the interfacial interaction with the plasma-deposited fluoropolymer film (see below), the topography of the pp-APFB film appears to be independent of the chemical states of the silicon surface. Figure 2b shows the AFM image of the nanostructured pp-APFB film deposited under the same glow discharge conditions on the hydrogen-terminated silicon (H–Si) surface. The size and size distribution ($D_m = 138$ nm, SD = 14 nm) of the nanospheres in this film are comparable to those of the nanospheres in the pp-APFB film of Figure 2a. The nanoporous structure of the pp-APFB film resulting from aggregation of the nanoparticles is revealed by the SEM image. Figure 3 shows the SEM cross-sectional image of the pp-APFB film deposited under the same conditions as those used for depositing the films of Figure 2. The nanoporous structure of the film is discernible in the cross-sectional view. The dark areas are the voids associated with the interstitial spaces of the agglomerated nanoparticles.

3.2. Chemical Composition of the pp-APFB Films. Figure 4 shows the respective C1s core-level spectra of the pp-APFB films on the pristine silicon substrates prepared at the constant system pressure of 800 mTorr and substrate temperature of 25

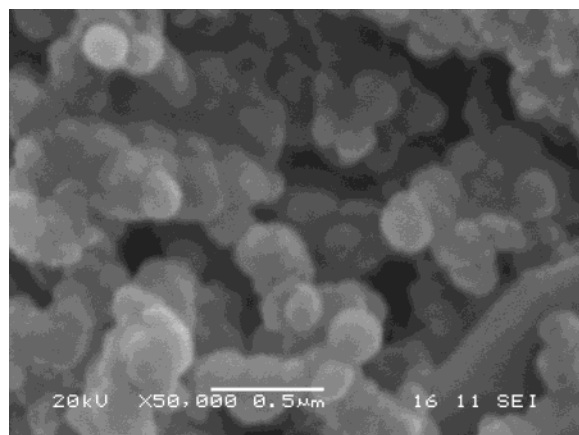


Figure 3. SEM cross-sectional images of the pp-APFB film deposited at 400 W, 800 mTorr, and 25 °C on the pristine silicon surface.

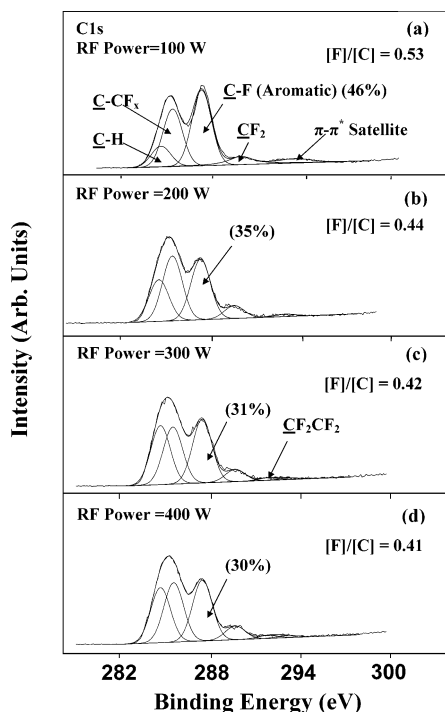


Figure 4. C1s core-level spectra of the pp-APFB films deposited on the pristine silicon surfaces at the system pressure of 800 mTorr and substrate temperature of 25 °C, but at the RF power of (a) 100, (b) 200, (c) 300, and (d) 400 W.

°C, but under the input RF power of 100 (part a), 200 (part b), 300 (part c), and 400 W (part d). The C 1s core-level spectra can be curve-fitted with peak components having binding energies (BEs) at 284.6 eV for the C–H species, at 285.2 eV for the C–CF_x (*x* = 1–3) species, at 287.2 eV for the CF (aromatic) species, at 289.8 eV for the CF₂ species, and at 291.8 eV for the CF₂CF₂ species.^{41–43} The broad peak at the higher BE of 293.2 eV is assigned to the π–π* shake-up satellite associated with the aromatic ring of the APFB unit.^{7,44}

The input RF power has a marked effect on the chemical composition of the resulting nanostructured pp-APFB film. The intensity of the peak components associated with the aromatic CF species and the π–π* shake-up satellite decreases with the increase in RF power. For the pp-APFB films obtained at the RF power 100 W, the proportion of the aromatic CF species is about 46% (compared to the theoretical composition of about 56% for the APFB molecule). As the RF power is increased to 200, 300, and 400 W, the proportion of the aromatic CF species

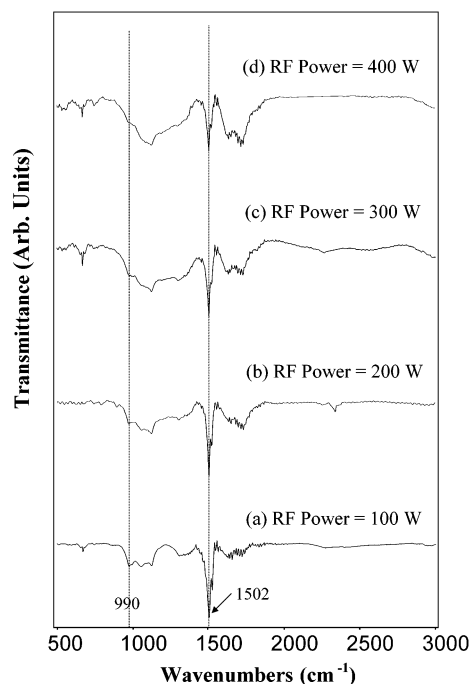


Figure 5. FTIR spectra of the pp-APFB films deposited on the pristine silicon surfaces at the system pressure of 800 mTorr and substrate temperature of 25 °C, but at the RF power of (a) 100, (b) 200, (c) 300, and (d) 400 W.

decreases to 35%, 31%, and 30%, respectively. The overall fluorine content, or the [F]/[C] ratio, decreases from 56% for the ideal APFB molecule to 53%, 44%, 42%, and 41% for the pp-APFB films deposited at the corresponding RF power of 100, 200, 300, and 400 W. On the other hand, the peak component associated with the CF₂CF₂ species is also discernible in the spectra of the films deposited at the RF power of 300 and 400 W. The variation in chemical composition of the pp-APFB films with the RF power probably arises from the difference in bond scission mechanism during the plasma polymerization process. The bond scission mechanism, in turn, is governed by the W/FM parameter,⁴⁵ where the W, F, and M are the input RF power, the monomer flow rate, and the molecular weight of the monomer, respectively. At a constant monomer flow rate and constant system pressure, the energy per unit mass of the molecule is low at the low RF power of 100 W. Thus, plasma polymerization proceeds under an energy-deficient state, and bond scission occurs mainly at the π bonds of the allyl groups, which have the lowest bond energy^{46,47} in the APFB molecule. Under this condition, rearrangement of the active radicals results in a plasma polymer having the similar chain structure as that of the APFB homopolymer. As the RF power is increased, more energy is available per unit mass of the monomer, leading to more severe molecular fragmentation. Under this condition, the APFB plasma has more active radicals, which come from scission of the π bonds, the allyl groups, the C–H bonds and the C–F bonds, as well as the scission and opening of the aromatic rings. The bond scissions involving the aromatic rings help to account for the reduction in fluorine content of the aromatic rings and the decrease in intensity of the π–π* shake-up satellite for the pp-APFB films deposited at the high RF power.

3.3. Chemical Structure of the pp-APFB Films. The input RF power also has a marked effect on the chemical structure of the pp-APFB films, because of the difference in the bond scission mechanism of the APFB monomer at different levels of the input RF power. Figure 5 shows the FTIR spectra of the

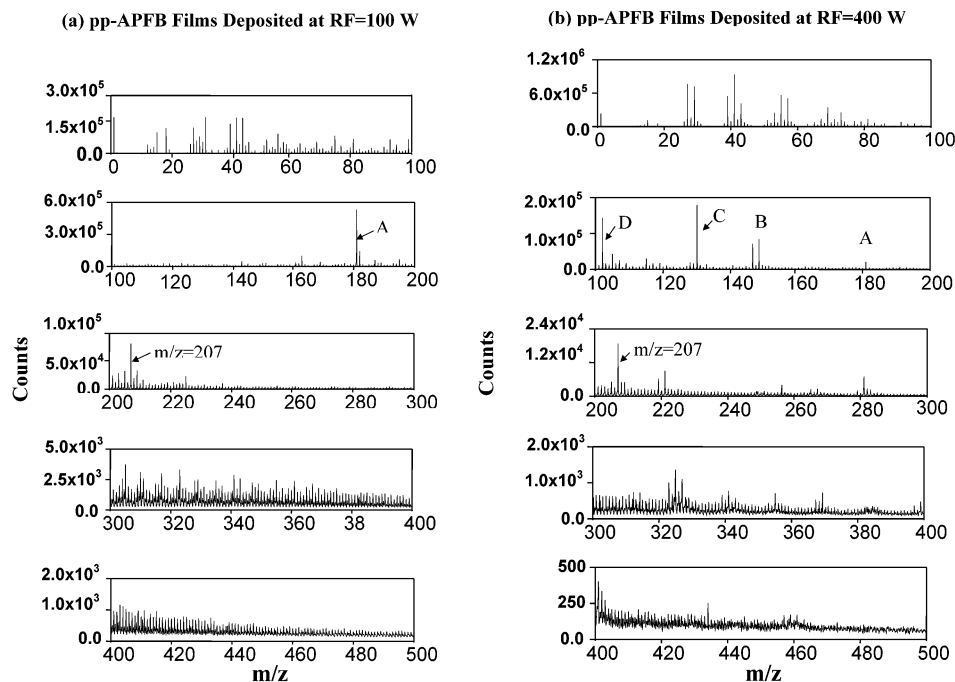
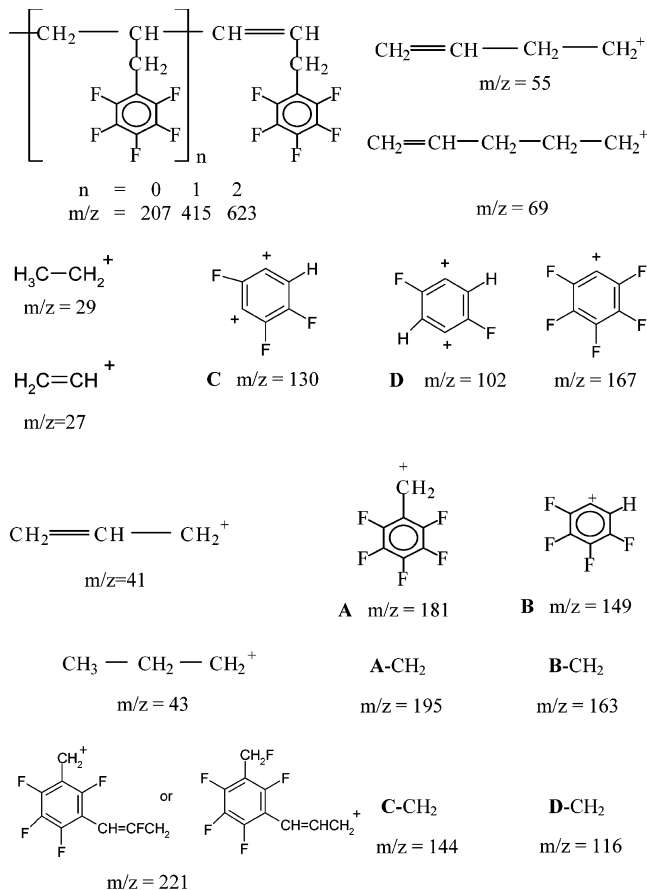


Figure 6. Positive ion ToF-SIMS spectra of the pp-APFB films on the pristine silicon substrates deposited at the system pressure of 800 mTorr and substrate temperature of 25 °C, but at the RF power of (a) 100 and (b) 400 W.

pp-APFB films deposited at the substrate temperature of 25 °C and system pressure of 800 mTorr, but at the RF power of 100 (part a), 200 (part b), 300 (part c), and 400 W (part d). The FTIR spectra of the pp-APFB films display the characteristic absorption bands of the C–F ring stretching vibrations at 990 cm^{-1} and of the C=C ring stretch at 1502 cm^{-1} .^{7,24,25} The absorption bands at 1100–1400 cm^{-1} arise from the overlap of the CF_x ($x = 1-3$) species.⁷ The weak bands between 700 and 900 cm^{-1} are associated with the vibrations of a mixture of *m*-, *p*-, and *o*-linked rings generated from defluorination of the aromatic rings of the APFB units.^{48–51} The FTIR results reveal that, with the increase in input RF power, the peak absorption intensity at 990 cm^{-1} and at 1502 cm^{-1} decreases, whereas the intensity of bands at 1100–1400 cm^{-1} is enhanced. Thus, with the increase in input RF power, the degree of defluorination of the APFB rings and the extent of formation of the complex aliphatic CF_x structure in the pp-APFB film are enhanced.

The ToF-SIMS spectra of the nanostructured pp-APFB films deposited on the pristine silicon substrates, under the system pressure of 800 mTorr and substrate temperature of 25 °C, but at different input RF powers of 100 and 400 W are shown in Figure 6, parts a and b, respectively. The assignment of the positive ion fragments of the pp-APFB films is shown in Scheme 1. The preservation of a substantial proportion of the fluorinated aromatic rings is indicated by the strong $\text{C}_6\text{F}_5\text{—CH}_2$ peak ($m/z = 181$, peak A). The relative peak intensities of the $\text{C}_6\text{F}_5\text{—CH}_2$ fragment and the APFB repeat unit ($m/z = 207$) for the pp-APFB film deposited at the RF power of 100 W are much higher than those of the corresponding species for the pp-APFB film deposited at the higher RF power of 400 W. At the lower input RF power of 100 W, the energy per monomer unit is low. Under this condition, the radical-initiated polymerization of APFB proceeds predominately via the carbon–carbon double bonds. The more linear polymer structures generated give rise to the well-preserved $\text{C}_6\text{F}_5\text{—CH}_2$ ($m/z = 181$) and $\text{C}_6\text{F}_5\text{—CH}_2\text{—CH=CH}_2$ ($m/z = 207$) fragments in the ToF-SIMS spectrum of the pp-APFB film. As the RF power is increased, more energy per

SCHEME 1: Assignments of Positive Ions in ToF-SIMS



APFB unit is available, leading to more severe molecular fragmentation. Thus, a more complex plasma polymerization mechanism, involving cross-linking and branching, sets in. In Figure 6b, the strong intensity of the peaks B, C, and D indicates that defluorination of the aromatic rings has occurred to a significant extent at the high RF power. The presence of

TABLE 2: Water Contact Angles of the pp-APFB Surfaces

RF power (W)	system pressure											
	200 mTorr			400 mTorr			600 mTorr			800 mTorr		
	R_a^a (nm)	Δt^b (μm)	$\theta_A^c \theta_R$	R_a (nm)	Δt (μm)	$\theta_A \theta_R$	R_a (nm)	Δt (μm)	$\theta_A \theta_R$	R_a (nm)	Δt (μm)	$\theta_A \theta_R$
100	626	1.7	160 \pm 3 134 \pm 2	592	1.3	158 \pm 3 139 \pm 2	565	1.2	156 \pm 5 138 \pm 2	442	1.2	150 \pm 3 136 \pm 4
200	474	1.3	143 \pm 3 116 \pm 3	401	1.3	141 \pm 3 118 \pm 3	386	1.2	134 \pm 2 116 \pm 3	323	1.2	123 \pm 2 118 \pm 3
300	362	1.2	134 \pm 2 92 \pm 2	292	1.5	125 \pm 3 86 \pm 4	204	1.3	118 \pm 3 84 \pm 2	128	1.0	113 \pm 3 83 \pm 4
400	234	1.3	124 \pm 2 76 \pm 2	265	1.3	118 \pm 2 74 \pm 3	152	1.4	113 \pm 1 75 \pm 2	74	1.3	99 \pm 4 77 \pm 4

^a The surface roughness value was obtained from the roughness profile of the AFM image. ^b Δt is the thickness of the pp-APFB film. ^c θ_A and θ_R are the advancing and receding water contact angle, respectively, in degrees.

fragments involving double ions, viz., the C, D, C-CH₂, and D-CH₂ species arising from the fragmentation of the cross-linked polymer, suggests that the nanostructured pp-APFB film deposited at the high RF power of 400 W contains a high proportion of cross-linked structures. The ToF-SIMS results are thus consistent with the FTIR and XPS results.

3.4. Interaction of the pp-APFB Film with the Hydrogen-Terminated Silicon. For the application of the pp-APFB film as a reliable dielectric or passivation layer on a silicon substrate, the deposited dielectric layer should exhibit good adhesion with the silicon substrate. One of the commonly used methods in the microelectronics industry for evaluating the adhesion of a film to a substrate is the Scotch tape peel test.¹ The interaction of the pp-APFB film with the hydrogen-terminated silicon (H-Si) surface and the pristine (native oxide-covered) silicon surface was evaluated by the Scotch tape peel test and the analysis of the chemical composition of the delaminated surfaces.

The adhesion strength of the pp-APFB films with the pristine silicon substrates is marginal (≤ 0.3 N/cm). The pp-APFB films generally exhibit good adhesion with the H-Si surface. The 180°-peel adhesion strength of the Scotch tapes with the pp-APFB films, deposited in the RF power range of 100–400 W, on the H-Si substrates increases from 0.9 to 1.3 N/cm. However, delamination occurs cohesively inside the pp-APFB film. The pp-APFB/H-Si interface remains intact after the Scotch tape peel test, as suggested by the results of chemical composition analysis of the delaminated surfaces (see below).

The interaction of the pp-APFB films with the silicon substrates was studied via XPS analysis of the delaminated interfaces. Figure 7, parts a and b, shows the respective wide scan spectra of the delaminated Scotch tape surfaces from the pp-APFB films deposited (RF power = 400 W, system pressure = 800 mTorr and substrate temperature = 25 °C), on the pristine silicon and H-Si surfaces. The spectra are grossly similar to each other, as well as to that of the original pp-APFB film. Figure 7, parts c and d, shows the corresponding wide scan spectra of the delaminated silicon substrate surfaces. A stronger Si signal intensity is observed for the delaminated pristine silicon surface. The Si signal of the delaminated H-Si surface, on the other hand, is obscured by the persistence of a thick pp-APFB layer after the peel test. The phenomena suggest that the delamination must have occurred inside the pp-APFB film and the pp-APFB film must have adhered strongly to the H-Si surface. The enhanced interfacial adhesion, in turn, arises from the chemical interaction at the polymer/substrate interface. The radical sites (dangling bonds) on the H-Si surface,⁵² formed by scission of the Si-H bonds during interaction with radicals and deep-UV in the plasma, probably have reacted with the activated species in the plasma to form the surface-bonded fluoropolymers. The Si 2p core-level spectrum in Figure 7d can

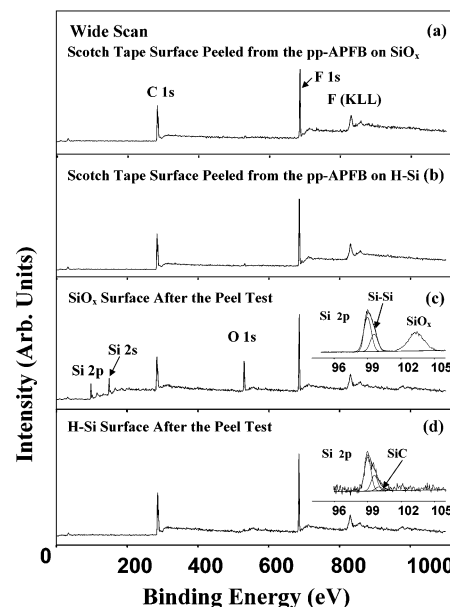


Figure 7. XPS wide scan spectra of the delaminated Scotch tape surfaces from the pp-APFB films deposited on the (a) pristine silicon and (b) H-Si surface. The corresponding spectra for the delaminated silicon substrate surfaces are shown in parts c and d.

be curve-fitted with two peak components having BEs at 99.2 eV for the Si-Si species and at 100.2 eV for the Si-C species.⁵³ The Si-C species probably resulted from reaction of the APFB fragments with the dangling bonds on the H-Si surface. It is also probable that the H-Si groups themselves react with the APFB monomer directly at the double bond.⁴⁰

3.5. Hydrophobic Nature of the Nanostructured pp-APFB Film. The nanostructured pp-APFB films are expected to exhibit a high degree of hydrophobicity. Table 2 summarizes the advancing and receding water contact angles of the pp-APFB films deposited under various glow discharge conditions. All of the films have a thickness on the order of 1–2 μm . AFM topographical images of the films suggest complete coverage of the substrate surfaces by the pp-APFB nanospheres. The advancing and receding water contact angle of the pp-APFB surface decrease with the increase in RF power and system pressure used for deposition. The decrease in water contact angle can be accounted for as follows. First of all, the surface water contact angle of the pp-APFB film is governed by its surface roughness, in addition to its surface composition. The surface roughness and the static water contact angle are related by the Wenzel's equation⁵⁴

$$\cos \theta^* = r \cos \theta$$

where θ^* , θ , and r are the apparent static contact angle of a solid surface, the true static angle of a geometrically “smooth” surface, and the roughness factor of the surface, respectively. The roughness is equal to 1 for a smooth surface and is always greater than 1 for the real surface. The hydrophobicity of a surface can be enhanced by increasing the roughness of a surface. The data in Table 2 show that, with the increase in RF power and system pressure, the surface roughness of the deposited pp-APFB films decreases, consistent with the observed decrease in water contact angle. At the same time, hydrophobicity of the pp-APFB film is also governed by its surface chemical composition. According to the results of the chemical composition and structure analysis of the pp-APFB films by XPS and ToF-SIMS, the extent of defluorination increases with the increase in RF power used for film deposition. Thus, the pp-APFB film deposited under the high RF power has a higher surface energy than that of the film deposited under the low RF power. For the pp-APFB film deposited at the high RF power and under high pressure, the decrease in both surface roughness and fluorine content has given rise to a surface water contact angle much lower than that of the ultra-hydrophobic pp-APFB film (with an advancing angle of $160 \pm 3^\circ$) obtained at the low RF power of 100 W and system pressure of 200 mTorr.

The contact angle hysteresis (the difference between the advancing and receding contact angle) can be regarded as the force required to move a liquid droplet across the surface. The smaller the contact angle hysteresis, the higher the surface hydrophobicity. The data in Table 2 show that the contact angle hysteresis of the pp-APFB film decreases with the increase in system pressure used for deposition. A more “composite surface” was obtained at the low system pressure. The changes in surface structure can be observed in the AFM images of Figure 1d–f. For the probing water droplet, a composite interface causes air to become trapped in the voids, preventing the liquid from penetrating and wetting the surface uniformly.^{55,56} The process is governed by a particular form of the Cassis-Baxter law which gives the contact angle of a composite surface⁵⁶

$$\cos \theta^* = -1 + \Theta_s(\cos \theta + 1)$$

in which Θ_s is the solid fraction of the surface and is itself a function of the contact angle θ . With the variation in surface chemical composition ([F]/[C] ratio) of the present pp-APFB films with surface topography and because the value of the actual fraction of solid in contact with water cannot be precisely determined for the present surface geometry, the roughness factor is estimated from the Wenzel's equation instead. For example, for the pp-APFB film deposited at 200 W and 800 mTorr (Table 2) and with a surface [F]/[C] ratio of 0.44 (Figure 4b), the roughness factor is determined to be about 3.0, based on the θ value of 103° for a relatively flat pp-APFB film surface of comparable [F]/[C] ratio from our earlier work.⁴¹ The data in Table 2 also show that the contact angle hysteresis increases with the increase in RF power. In addition to the decrease in surface roughness, this phenomenon can be partially explained by the fact that severe defluorination occurred in the pp-APFB films deposited under high RF power. The higher the fluorine content of the pp-APFB film, the lower the surface energy. The lower surface energy, in turn, gives rise to less hysteresis in the contact angles.⁵⁷

4. Conclusions

Nanoporous and highly hydrophobic fluoropolymer films composed of nanospheres were deposited on the oxide-covered

and hydrogen-terminated Si(100) surfaces via plasma polymerization of allylpentafluorobenzene (APFB). The chemical composition and structure, as well as the physical morphology (size and size distribution of the nanospheres), of the plasma polymerized APFB (pp-APFB) films could be controlled to a large extent by the glow discharge conditions, such as RF power, system pressure and substrate temperature. The reactive nature of the dangling bonds on the hydrogen-terminated silicon (H–Si) surface had given rise to strong interaction between the pp-APFB film and the silicon substrate. As a result, good adhesion of the pp-APFB film to the H–Si surface was achieved.

References and Notes

- (1) Maier, G. *Prog. Polym. Sci.* **2001**, *26*, 3.
- (2) Nalwa, H. S. *Handbook of Low and High Dielectric Constant Materials and Their Application: Materials and Processing*; Academic Press: San Diego, CA, 1999; p 4.
- (3) Martin, S. J.; Godschalk, J. P.; Mills, M. E.; Shaffer, E. O., II; Townsend, P. H. *Adv. Mater.* **2000**, *12*, 1769.
- (4) Rajagopal, A.; Gregoire, C.; Lemaire, J.; Pireaux, J. J.; Bakanov, M. R.; Vanhaelemeersch, S.; Maex, K. *J. Vac. Sci. Technol. B* **1999**, *17*, 1.
- (5) Sacher, E. *Prog. Surf. Sci.* **1994**, *47*, 273.
- (6) Endo, K.; Shinoda, K.; Tatsumi, T. *J. Appl. Phys.* **1999**, *86*, 2739.
- (7) Mackie, N. M.; Castner, D. G.; Fisher, E. R. *Langmuir* **1998**, *14*, 1227.
- (8) Butoi, C. I.; Mackie, N. M.; Gamble, L. J.; Castner, D. G.; Barnd, J.; Miller, A. M.; Fisher, E. R. *Chem. Mater.* **2000**, *12*, 2014.
- (9) Coulson, S. R.; Woodward, I. S.; Badyal, J. P. S.; Brewer, S. A.; Willis, C. *J. Phys. Chem. B* **2000**, *104*, 8836.
- (10) Limb, S. J.; Edell, D. J.; Gleason, E. F.; Gleason, K. K. *J. Appl. Polym. Sci.* **1998**, *67*, 1489.
- (11) Ingaki, N.; Tasaka, S.; Mase, T. *J. Appl. Polym. Sci.* **1989**, *37*, 2341.
- (12) Oehr, C.; Suhr, H. *Thin Solid Films* **1987**, *155*, 65.
- (13) Jiang, H.; Johnson, W. E.; Grant, J. T.; Eyink, K.; Johnson, E. M.; Tomlin, D. W.; Bunning, T. J. *Chem. Mater.* **2003**, *15*, 340.
- (14) Marthai, C. J.; Saravanan, S.; Anantharaman, M. R.; Venkkitachalam, S.; Jayalekshmi, S. *J. Phys. D: Appl. Phys.* **2002**, *35*, 240.
- (15) Han, L. M.; Timmons, R. B. *J. Appl. Phys.* **1998**, *84*, 439.
- (16) Leezenberg, P. B.; Reiley, T. C.; Tyndall, G. W. *J. Vac. Sci. Technol.* **1999**, *17*, 275.
- (17) Durrant, S. F.; Castro, S. G. C.; Bolvar-Marinez, L. E.; Galvao, D. S.; de Moraes, M. A. B. *Thin Solid Films* **1997**, *304*, 149.
- (18) Coulson, S. R.; Woodward, I. S.; Badyal, J. P. S.; Brewer, S. A.; Willis, C. *Langmuir* **2000**, *16*, 6287.
- (19) Sandrin, L.; Silverstein, M. S.; Sacher, E. *Polymer* **2001**, *42*, 3761.
- (20) Hadjadj, M. A.; Beorchia, A.; Cabarocas, P. R.; Boufendi, L.; Huet, S.; Bunbendorff, J. L. *J. Phys. D: Appl. Phys.* **2001**, *34*, 690.
- (21) Loo, L. S.; Gleason, K. K. *Electrochem. Solid-State Lett.* **2001**, *4*, G81.
- (22) Kohl, P. A.; Bhusarin, D. M.; Wedlake, M. *IEEE Electron. Device* **2000**, *L21*, 557.
- (23) Hedrick, J. L.; Carter, K. R.; Labadie, J. W.; Miller, R. D.; Volksen, W.; Hawker, C. J.; Yoon, D. Y.; Russell, T. P.; McGrath, J. E.; Briber, R. M. In *Progress In Polyimide Chemistry I&II*; Kricheldorf, H. R., Ed.; Springer-Verlag: New York, 1999; p 11.
- (24) Nguyen, C. V.; Carter, K. R.; Hawker, C. J.; Hedrick, J. L.; Jaffe, R. L.; Miller, R. D.; Remedar, J. F.; Rhee, H. W.; Rice, P. M.; Toney, M. F.; Trollsas, M. T.; Yoon, D. Y. *Chem. Mater.* **1999**, *11*, 3080.
- (25) Padovani, A. M.; Rhodes, L.; Riestler, L.; Lohman, G.; Tsuie, B.; Conner, J.; Bistrup, S. A.; Kohl, P. A. *Electrochem. Solid-State Lett.* **2001**, *4* (11), 25.
- (26) Su, R. Q.; Müller, T. E.; Prochazka, J.; Lercher, J. A. *Adv. Mater.* **2002**, *14*, 1369.
- (27) Kim, H. C.; Wilds, J. B.; Kreller, C. R.; Volksen, W.; Brock, P. J.; Lee, V. Y.; Magbitang, T.; Hedrick, J. L.; Hawker, C. J.; Miller, R. D. *Adv. Mater.* **2002**, *14*, 1637.
- (28) McWhirter, R. J. *Energy Res. Abs.* **1981**, *6*, 2627.
- (29) Gagliani, J.; Supkis, D. E. *Adv. Astronaut. Sci.* **1979**, *38*, 193.
- (30) Hedrick, J. L.; Labadie, J. W.; Russell, T. P.; Hofer, D.; Wakharkar, V. *Polymer* **1993**, *34*, 4717.
- (31) Meyers, R. A. *J. Polym. Sci. Part A: Polym. Chem.* **1969**, *7*, 2757.
- (32) Hedrick, J. L.; Dipietro, R.; Charlier, Y.; Jerome, R. *High Perform. Polym.* **1995**, *7*, 133.
- (33) Takahashi, K.; Tachibana, K. *J. Vac. Sci. Technol. A* **2001**, *19* (5), 2055.
- (34) Berndt, J.; Hong, S.; Kovacevic, E.; Stefanovic, I.; Winter, J. *Vacuum* **2003**, *71*, 377.

- (35) Boufendi, L.; Plain, A.; Blondeau, J. Ph.; Bouchoule, A.; Laure, C.; Toogood, M. *Appl. Phys. Lett.* **1992**, 60 (2), 169.
- (36) Boufendi, L.; Herman, J.; Bouchoule, A.; Dubreuil, B. *J. Appl. Phys.* **1994**, 76 (1), 148.
- (37) Teare, D. O. H.; Spanos, C. G.; Ridley, P.; Kinmond, E. J.; Rouccoules, V.; Badyal, J. P. S. *Chem. Mater.* **2002**, 14, 4566.
- (38) Hahn, H.; Averback, R. S. *J. Appl. Phys.* **1990**, 67, 1113.
- (39) Chen, X. L.; Rajeshwar, K.; Timmons, R. B. *Chem. Mater.* **1996**, 8, 1067.
- (40) Buriak, J. M. *Chem. Rev.* **2002**, 102, 1271.
- (41) Yang, G. H.; Zhang, Y.; Kang, E. T.; Neoh, K. G.; Huan, A. C. H.; Lai, D. M. Y. *J. Mater. Chem.* **2002**, 12, 426.
- (42) Zhang, Y.; Kang, E. T.; Neoh, K. G.; Huang, W.; Huan, A. C. H.; Zhang, H.; Lamb, R. N. *Polymer* **2002**, 43, 7279.
- (43) Clark, D. T.; Brennan, W. J. *J. Fluorine Chem.* **1988**, 40, 419.
- (44) Muilenberg, G. E. *Handbook of X-ray Photoelectron Spectroscopy*; Perkin-Elmer Corporation: Eden Prairie, MN, 1978; p 38.
- (45) Yasuda, H.; Hirotsu, T. *J. Polym. Sci. Polym. Chem. Ed.* **1978**, 16, 743.
- (46) Huhey, J. E. *Inorganic Chemistry*, 2nd ed.; Harper and Row: New York, 1978; Appendix F.
- (47) Morgon, M.; Ryan, E. T.; Zhao, J. H.; Hu, C. *Annu. Rev. Mater. Sci.* **2000**, 30, 645.
- (48) Han, L. M.; Timmons, R. B. *Vac J. Sci. Technol. B* **2000**, 18 (2), 799.
- (49) Durrant, S. F.; Mota, R. P.; de Moraes, M. A. B. *Thin Solid Films* **1992**, 220, 295.
- (50) Jesch, K.; Blear, J. E.; Kronick, P. L. *J. Polym. Sci.* **1996**, 4, 1487.
- (51) Seeger, M.; Gritter, R. J.; Tibbitt, J. M.; Shen, M.; Bell, A. T. *J. Polym. Sci., Polym. Chem. Ed.* **1997**, 15, 1403.
- (52) Cicero, R. L.; Linford, M. R.; Chidsey, C. E. D. *Langmuir* **2000**, 16, 5689.
- (53) Diani, M.; Diouri, J.; Kubler, L.; Simon, L.; Aubel, D. *Surf. Rev. Lett.* **2003**, 10 (1), 55.
- (54) Good, R. J. *J. Am. Chem. Soc.* **1952**, 74, 5041.
- (55) Cassie, A. B. D.; Baxter, S. *Trans. Faraday Soc.* **1994**, 3, 16.
- (56) Bico, J.; Marzolin, C.; Quere, D. *Europhys. Lett.* **1999**, 47 (2), 220.
- (57) Chibowski, E. *Adv. Colloid Interface Sci.* **2003**, 103, 149.